Oblique shock structures formed during the ablation phase of aluminium wire array z-pinches

G. F. Swadling, S. V. Lebedev, N. Niasse, J. P. Chittenden, G. N. Hall et al.

Citation: Phys. Plasmas **20**, 022705 (2013); doi: 10.1063/1.4790520
View online: http://dx.doi.org/10.1063/1.4790520
View Table of Contents: http://pop.aip.org/resource/1/PHPAEN/v20/i2
Published by the American Institute of Physics.

Oblique shock structures formed during the ablation phase of aluminium wire array z-pinches

G. F. Swadling, S. V. Lebedev, N. Niasse, J. P. Chittenden, G. N. Hall, F. Suzuki-Vidal, G. Burdiak, A. J. Harvey-Thompson, S. N. Bland, P. De Grouchy, E. Khoory, L. Pickworth, J. Skidmore, and L. Suttle
The Blackett Laboratory, Imperial College, London SW7 2BW, United Kingdom

(Received 7 December 2012; accepted 14 January 2013; published online 8 February 2013)

A series of experiments has been conducted in order to investigate the azimuthal structures formed by the interactions of cylindrically converging plasma flows during the ablation phase of aluminium wire array Z pinch implosions. These experiments were carried out using the 1.4 MA, 240 ns MAGPIE generator at Imperial College London. The main diagnostic used in this study was a two-colour, end-on, Mach-Zehnder imaging interferometer, sensitive to the axially integrated electron density of the plasma. The data collected in these experiments reveal the strongly collisional dynamics of the aluminium ablation streams. The structure of the flows is dominated by a dense network of oblique shock fronts, formed by supersonic collisions between adjacent ablation streams. An estimate for the range of the flow Mach number ($M = 6.2$-9.2) has been made based on an analysis of the observed shock geometry. Combining this measurement with previously published Thomson Scattering measurements of the plasma flow velocity by Harvey-Thompson *et al*. [Physics of Plasmas **19**, 056303 (2012)] allowed us to place limits on the range of the $\bar{Z}T_e$ of the plasma. The detailed and quantitative nature of the dataset lends itself well as a source for model validation and code verification exercises, as the exact shock geometry is sensitive to many of the plasma parameters. Comparison of electron density data produced through numerical modelling with the Gorgon 3D MHD code demonstrates that the code is able to reproduce the collisional dynamics observed in aluminium arrays reasonably well. © *2013 American Institute of Physics*. [http://dx.doi.org/10.1063/1.4790520]

I. INTRODUCTION

Pulsed-power driven wire array Z-pinch implosions (recently reviewed by Haines 2011[1]) are capable of efficiently generating powerful bursts of X-ray radiation. They have been used extensively to drive experiments in research fields such as inertial confinement fusion (ICF), high energy density physics (HEDP), and laboratory astrophysics. Experiments at the 20 MA Z facility at Sandia National Laboratories have produced pulses of soft x-ray radiation with a peak power of 280 TW and a total yield of 1.8 MJ.[2]

The dynamics of wire array implosions have been studied over a wide range of drive parameters. Generally, it is possible to divide the evolution of their dynamics into a set of four discrete phases; initiation, ablation, implosion, and stagnation.[3–5]

During the initiation phase, the wires are heated ohmically, causing them to vaporise and expand. The wires electrically break down and a heterogeneous structure is formed; the wire cores remain relatively cold, dense and resistive, but are surrounded by sheaths of hot, low density, highly conductive coronal plasma. The lower resistivity of this coronal plasma ensures that it carries the majority of the drive current.

During the ablation phase the $\vec{J} \times \vec{B}$ interaction between the current carrying corona and the array's global self-magnetic field results in a force which acts to accelerate the coronal plasma towards the axis, leading to the formation of ablation streams emanating from each of the wire cores. The mass swept away from the coronae by this process is replenished via further ablation of the dense cores. The ablation phase takes up a significant portion of the total dynamic time; in 1 MA experiments the ablation phase has been shown to account for ~80%[3] of the total experimental time, and at the 20 MA scale ~65%[4] (240 ns and 100 ns drive periods, respectively). The ablation process continues until approximately half of the initial wire mass has been removed from the wire cores, at which point breaks start to form in the wires. The breaks form at this time due to the highly non-uniform ablation rate along the length of the wires; the ablation rate is modulated at a predictable "fundamental" wavelength.[6,7] Once the wires are broken the array undergoes a snowplough like implosion,[8,9] followed by the stagnation of the accrued kinetic energy as an intense pulse of soft x-ray radiation.[10,11]

This paper presents the results of a series of experiments conducted in order to investigate the dynamics of wire array plasmas during the ablation phase. In particular, it focuses on the azimuthal ablation flow structures formed in aluminium wire arrays. The experiments were carried out using the 1.4 MA, 240 ns MAGPIE[12] pulsed power facility at Imperial College London. The main diagnostic used in these experiments was an end-on laser imaging interferometer. An end-on orientation was selected as it provides an unobstructed view of the array interior; for a side-on view the fringe pattern is normally interrupted by the dense wire cores, making

it impossible to trace fringes through the entire image. This orientation also suits the geometry of the wire array, as, apart from the "fundamental" modulation of the ablation rate, the dynamics are fairly axially uniform. While end on shadowgraphy and interferometry diagnostics have be fielded in previous experiments,[3,6,13,14] the work presented in this paper represents a significant improvement, both in terms of the apparatus used and the analysis techniques employed.

The main results of the work are summarised as follows: For the majority of the current drive period, the ablation flow appears to be highly collisional, with the structure observed appearing to be dominated by a network of oblique shocks. Analysis of the geometry of these shocks in 32 wire (8 mm radius) arrays allows us to place estimates on flow parameters such as the Mach number, and these estimates can then be compared with the results of numerical modelling.

In both the 16 and 32 wire data, we see evidence of hollow density profiles in the shocked regions formed by the collision of material flowing directly from the wire cores. It is suggested that these structures may be the result of higher temperature and therefore increased thermal pressure in the centre of these regions. Data from early times suggest that there may be a period of non-collisional flow. Calculations suggest the key driver for the change in the collisional regime of the plasma is the increasing density of the ablation plasma as the drive current increases.

The structures observed in the experimental data broadly agree with those seen in the results of numerical simulations using the Gorgon[15,16] MHD code, but with some differences in the exact flow parameters. It is thought that these differences may be due to Non-Local Thermodynamic Equilibrium (Non-LTE) effects in the experiment, which lead to reduced average ionisation state ($\bar{Z}$) of the plasma compared with that predicted by the LTE Thomas-Fermi ionisation model currently used in Gorgon.

The experimental dataset as a whole provides a detailed source for model validation and code verification exercises. The large body of quantitative measurements is well suited for detailed comparison with the results of numerical modelling. It should be noted that the discrepancy in the array behaviour from that predicted by simulation is much greater in the case of tungsten wire arrays. It is thought that this is due to reduced collisionality between the tungsten plasma streams, which results in non-fluid behaviour. The dynamics of these arrays will be discussed in detail in a separate publication.

The remainder of this paper is structured as follows. Section II describes the experimental setup and data analysis process. Section III presents experimental results, some discussion of the physics, estimates of fluid parameters and comparisons with Gorgon modelling. Section IV presents the conclusions.

II. EXPERIMENTAL SETUP AND ANALYSIS

A. Apparatus

Experiments were carried out using the MAGPIE generator at Imperial College London.[12] MAGPIE is a pulsed power driver, delivering a peak current of 1.4 MA with a rise time of ~240 ns and drive impedance of ~1.25 Ω.

The experiments described in this paper were conducted using aluminium cylindrical wire arrays, with wire numbers varying between 7 and 32 wires. These arrays all had radii of 8 mm and lengths of 10 or 20 mm. As the experiments focused on the investigation of plasma flow dynamics during the ablation phase, the arrays were designed to be overmassed, suppressing the implosion and stagnation phases. The reasons for this choice were twofold; first, the adverse effects of background radiation on the diagnostic suite are minimised, and second, the reduction in stagnated energy and thus x-ray yield results in reduced wear to the array hardware. Typical diameters for wires used in these arrays were 25–30 μm, similar to the diameters of wires used in aluminium array experiments on the Saturn[17] Generator at Sandia National Laboratories.

The main diagnostic used in this work was an end-on imaging interferometer. In an end-on orientation, the diagnostic has an axially (z) integrated view of the radial/azimuthal (r, θ) plane of the array. The interferometer uses two different probing wavelengths, with a variable inter-frame delay (0–24 ns), allowing it to capture two frames during each experiment. This is particularly useful for investigating the dynamics of the experiment. The experimental hardware was modified in order to provide better access for the end-on probing beam. In previous experiments,[3,6] a Michelson-Morley type probing arrangement has been used; the probing beam was directed down the axis of the array and reflected back through the array by a mirror mounted in the base of the cathode. The probing beam thus made two passes of the plasma. For the experiments reported in this paper a Mach–Zehnder scheme was used instead, a schematic of which is shown in Fig. 1(a). The two probe beams, combined together using a dichroic mirror, are directed down the axis of the array and reflected out through a hole in the side of the cathode. As a result, the probing beams make only a single pass through the wire array. This has a number of advantages. First, the alignment of the optics is greatly simplified; in a two pass scheme great care must be taken when aligning the cathode mounted mirror and the probing beam in order to avoid producing a double image. Second, the sensitivity of the interferometer is reduced by a factor of two, which is useful as the plasmas investigated in these experiments often contain strong density gradients, inducing large fringe shifts over short spatial scales. Third, the total effective optical length of the object is reduced to less than half of that in the double pass case (in the double pass case the imaging system must be focused on the cathode mirror, not the centre of the plasma, as this will effectively be the centre of the extended object). As a result of this a much higher quality of focus can be achieved at the imaging plane, reducing the strength of any unwanted shadowgraphy effects (brightening and darkening of the image around strong gradients), which can cause confusion with the interpretation of the fringe patterns.

Fig. 1(b) shows a schematic of the laser probing optical layout. The probing system uses the 2nd (532 nm) and 3rd (355 nm) harmonics of a SBS compressed, pulsed Nd:YAG laser. The time resolution of the probing line is set by the pulse duration of the laser to ~500 ps. The interferograms were captured using off-the-shelf Canon DSLRs; the camera

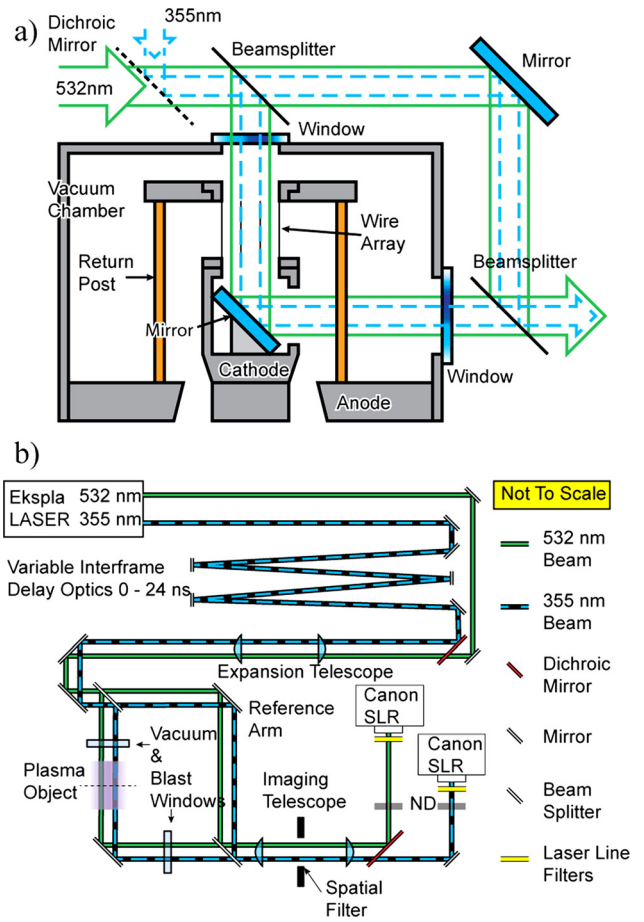

FIG. 1. (a) A schematic of the experimental setup used for the end-on laser interferometer. This is a two colour system, using the 2nd and 3rd Nd:YAG harmonics (532 and 355 nm). (b) Schematic of overall the optical setup used for the end-on laser probing system.

shutters were held open for the duration of the experiment. Neutral density (ND) filters are used to reduce the intensity of probing light reaching the camera's CCD and laser line filters are used in order to exclude the majority of the background plasma self-emission from the images. As already mentioned, two interferograms are captured during each experiment. The relative timing of these interferograms is controlled by a variable time-of-flight delay system, allowing the inter-frame delay to be set between 0 and 24 ns. The 355 nm probe is less sensitive to the electron density of the plasma and thus is capable of probing to higher densities than the 532 nm beam. As such the 355 nm beam is normally used as the later probe.

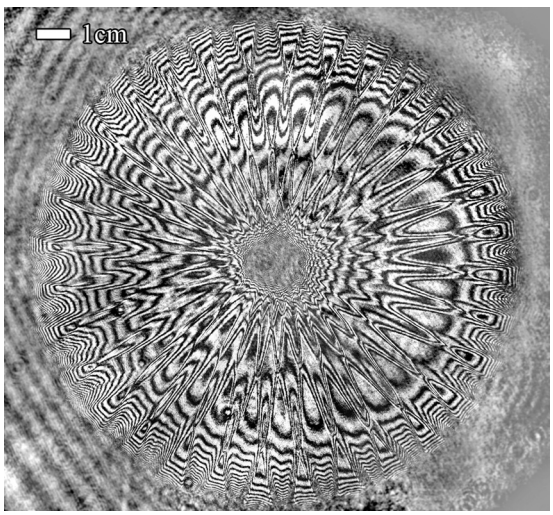

FIG. 2. An example of an interferogram captured during a 32 wire aluminium array experiment, at 142 ns, using the 532 nm probe. Note the extremely complex fringe pattern; it is difficult to interpret the data directly from the fringe pattern.

B. Analysis of interferograms

The end-on interferograms captured during these experiments proved to be extremely complex. Fig. 2 shows an example, captured during a 32 wire experiment. This complexity was one of the key drivers behind the development of the analysis tools described in this section.

A purpose build computer analysis tool "MAGIC"[18] was developed. The process of analysis is illustrated in Fig. 3. Fig. 3(a) shows a pair of raw reference (in the absence of plasma, left) and shot (with plasma, right) interferograms. A reference interferogram is captured before the start of the experiment for each wavelength. The reference fringe pattern is important as it provides information about the relative phase of the probe

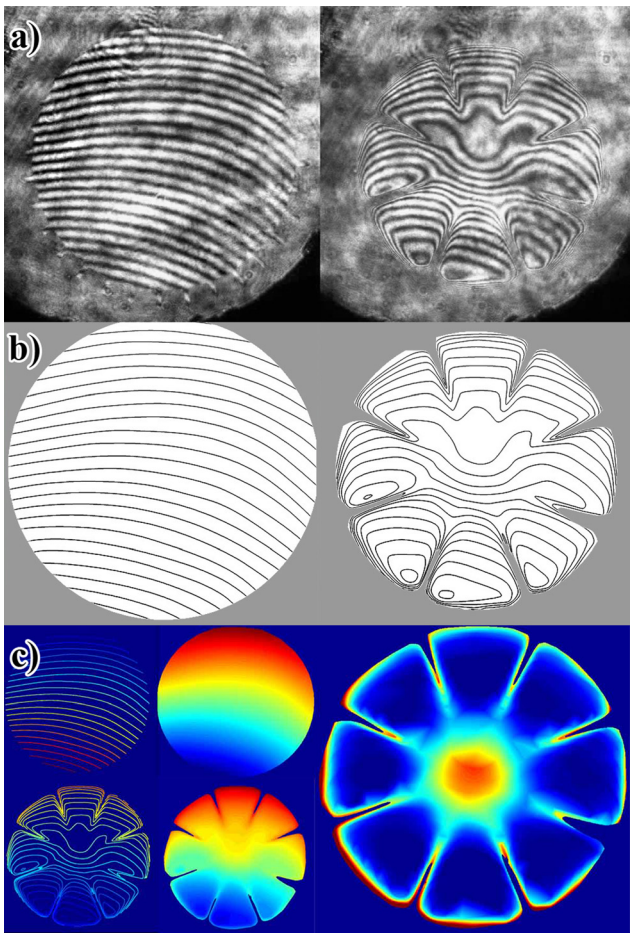

FIG. 3. An overview of the analysis process for interferograms. (a) Raw reference (left) and shot (right) interferograms. (b) Fringe minima are traced and formatted images produced. (c) Fringes are assigned relative indices, the regions between the fringes are interpolated, and the background phase is subtracted, leaving only the phase due to the plasma itself. This fringe map is then calibrated to extract the line averaged electron density.

and reference beam in the absence of any plasma object. Whilst ideally these reference fringes should form a set of straight, equally spaced, parallel lines, they are often distorted due to imperfections in the imaging optics, distortions in the vacuum and blast windows of the experimental chamber and small differences in the lengths of the two arms of the interferometer. Analysis the reference pattern allows us to subtract out these effects from the final data. The positions of the fringe intensity minima in the two interferograms are traced using image editing software. Once the positions of all of the fringes have been traced a pair of specially formatted image files are produced, as shown in Fig. 3(b).

These images are loaded into the analysis program, which scans them and identifies the individual fringes. It then assists the user in assigning numbers to the fringes in the correct order. The fringe patterns captured during these experiments are often extremely complex. In these cases, assignment of the correct fringe order required a degree of interpretation on the part of the user. The results of the numbering process are shown on the left hand side of Fig. 3(c) (expressed using colour-scaled contours). Once numbers have been assigned to all of the fringes, the analysis program interpolates fringe shift values for the spaces between the fringe positions in each image using a 2D linear interpolation routine. This results in the two images shown in the centre of Fig. 3(c). The fringe-shift introduced by the plasma object can then be calculated by subtracting the reference fringe shift from the shot fringe-shift map, leaving the data shown in the right-hand panel of Fig. 3(c) (In these images regions of high density/gradients which have obscured the probe beam have been masked).

The final step of the analysis process is to calibrate the fringe shift map in terms of the plasma electron density. For this step, it is assumed that the refractive index of the plasma is dominated by the contribution of the free-electrons. The refractive index (η_p) due to the free electrons is given by the following expression:[19]

$$\eta_p = \left(1 - \frac{n_e}{n_c}\right)^{\frac{1}{2}} \approx \ 1 - \frac{n_e}{2n_c}, \tag{1}$$

where n_e is the plasma electron density and n_c is the well-known critical electron density for the specific probing wavelength. The fringe shift (N_F) due to the effects of the plasma at any particular point in the image can be calculated using the following equation:

$$N_F(x,y) = \frac{1}{\lambda}\int_0^L \eta_p \ (x,y,z)dz - \frac{L}{\lambda}, \tag{2}$$

where λ is the probing wavelength and L is the length of the probing path (typically 10 or 20 mm). Substitution and rearrangement results in the following equation:

$$\int_0^L n_e(x,y,z)dz = -2n_c\lambda N_F(x,y). \tag{3}$$

The areal electron density per fringe shift is thus $-2n_c\lambda$. This is $-6.3\times10^{17}\,\mathrm{cm}^{-2}$ for a 355 nm probe and $-4.2\times10^{17}\,\mathrm{cm}^{-2}$ for a 532 nm probe. The average electron density can be found by dividing by the array length

$$\int_0^L n_e(x,y,z)dz = \langle n_e(x,y)\rangle L,$$
$$\langle n_e(x,y)\rangle = -\frac{2n_c\lambda}{L}N_F(x,y). \tag{4}$$

It should be noted that $\langle n_e(x,y)\rangle$ only represents the axially averaged electron density. Previous work has demonstrated that the ablation rate along the length of the wires is modulated at a characteristic "fundamental" wavelength,[3,13] driven by a modified form of the m = 0 plasma instability[20] (for aluminium this wavelength is $\lambda_f(Al) \sim 0.5$ mm[7]). Apart from this modulation, the overall dynamics of cylindrical wire arrays appear to be fairly uniform along their length. The modulation wavelength is much smaller than the array length and previous work has shown that the modulation of the ablation streams loses contrast over a scale of a few mm.[21] Therefore, the line averaged density should give a good handle on the global dynamics of the array.

III. DATA AND ANALYSIS

Fig. 4 contains plots of electron density distribution extracted via analysis of interferograms captured during experiments with 16 (a) and 32 (b) wires, respectively. In these plots, the initial wire positions are marked by red circles, and it should be noted that the field of view here has been limited to a radius of ~7 mm by dense plasma expanding off the wire mounting hardware. The regions coloured dark blue in these plots correspond to regions where the probing beam has been obscured, either by the array hardware, absorption in the dense plasma or by deflection out of the optical probing system due to strong refractive index gradients.

A. Shock structure in 32 wire aluminium arrays

The electron density structure is easiest to interpret in the 32 wire case (Fig. 4(b)). This plot is dominated by a network of sharp discontinuities in the electron density distribution, which are interpreted as oblique shock fronts. Working from the outside in, we see that the regions of highest density at the outer edges of the plot are aligned with the inter-wire gaps. This is somewhat surprising, as it might be expected that the highest density regions would correspond to the positions of the ablation streams flowing directly from the wire cores. In fact, these high density regions appear to be formed by the supersonic collision of material ablated directly from the wire cores on either side. This observation implies that the initial ablation streams are characterised by a large expansion angle, an interpretation which is supported by data from experiments on arrays with fewer wires, such as the interferogram shown in Fig. 5. This interferogram was captured during an experiment on a 7 wire aluminium array; modifications to the wire mounting hardware for this experiment allowed us to probe all the way out to the initial wire positions. Here, we see that the ablation streams have expanded to a maximum width of ~2.5 mm. Comparing this

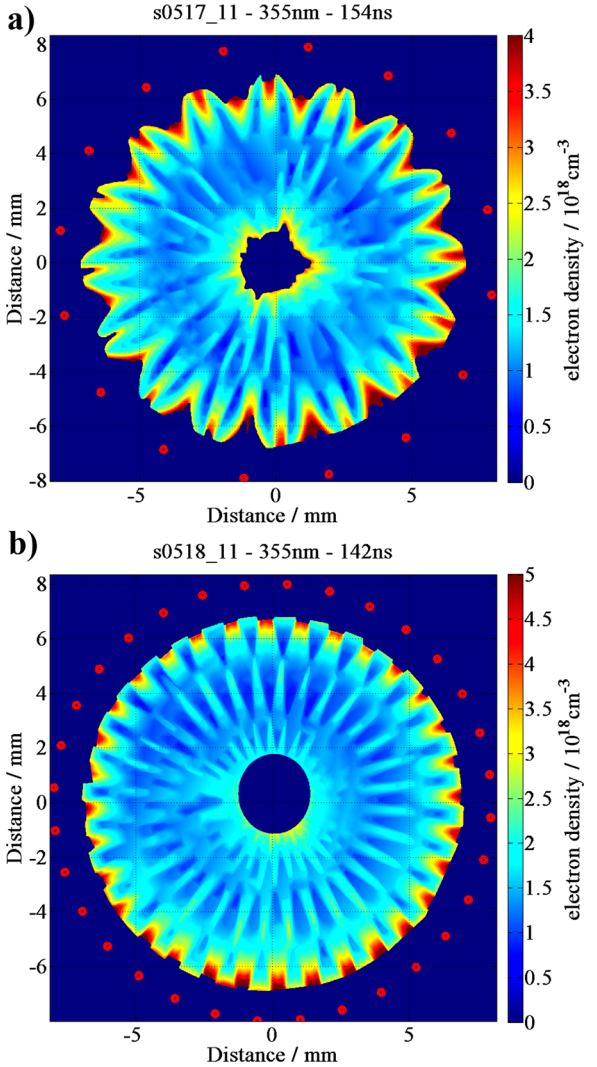

FIG. 4. Typical examples of electron density distributions for aluminium wire arrays. (a) 16 wire array. (b) 32 wire array. These plots are the result of the analysis of the raw interferograms, using the methods described in Sec. II B. In these plots, the dark blue/black regions correspond to regions where the probing beam has been obscured by the plasma. The red circles in this plot mark the initial wire positions.

with the initial interwire separation of ~1.6 mm in the case of a 32 wire array, it is not surprising that a significant portion of the ablation mass has been swept into this interwire shock region.

Fig. 6(a) shows a schematic of our interpretation of the collisional flow structure overlaid on an expanded view of a region of data from Fig. 4(b). As discussed above, the initial regions of highest density are formed by the supersonic collision of ablated material expanding directly from the wire cores. These regions, henceforth referred to as the "primary" shock regions, are bounded on either side by sharp discontinuities in the free electron density, corresponding to pairs of oblique shock fronts (marked by dashed white lines). Material crossing these shock fronts undergoes a change in its direction of flow such that the downstream flow vector runs parallel to the centreline of the shock region.

After material has passed into the primary shock region, it continues to propagate towards the axis. The width of the shocked region gradually increases towards the axis, as more

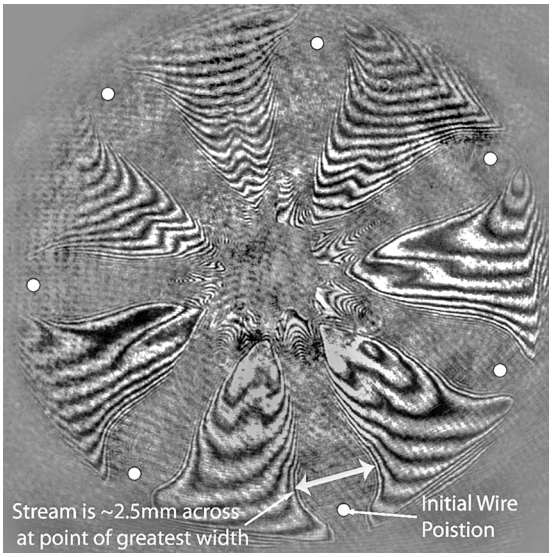

FIG. 5. An interferogram captured during an experiment on a 7 wire, 8 mm radius aluminium array. This image illustrates the wide ablation streams formed by aluminium arrays at low wire number. At higher wire number these stream begin to overlap and interact with one another.

and more of the initial ablation flow collides into it. Eventually, the primary shocks expand to the point where they have accrued all of the material from the initial ablation flows. Adjacent primary shocks then begin to collide into one another, leading to the formation of the "secondary" shock regions. As before, these regions are bounded on either side by oblique shock fronts, and their width increases towards the axis as material from the primary shocks continues to collide. As the primary shock material crosses the bounding oblique shock fronts its flow vector is again turned such that it now flows parallel to the centreline of the secondary shock region.

This process repeats again, leading to the formation of "tertiary" shocks, driven by the collision of adjacent secondary shock regions. There is even some evidence in the dataset of the formation of "quaternary" shock regions. This series of staged oblique shocks appears to be the main mechanism mediating the radial convergence of the array mass as it approaches the array axis. The electron density of the ablation flows roughly doubles as it passes through each shock front in turn. This process results in a highly non-uniform distribution of the prefill mass, which may affect the implosion stage, azimuthally modulating the time taken for the implosion front to reach the array axis.

B. Estimating the Mach number based on measurements of the shock geometry in 32 wire arrays

The shock front formed between the primary and secondary shock regions in the 32 wire data shown in Fig. 6(a) presents an opportunity for further analysis. For this interface, the directions of both the up-stream and down-stream flow vectors are well-defined, flowing parallel on each side of the interface along its full length (each flow is parallel however the flows on either side of the shock interface are at different angles). This makes it much easier to interpret than the interface between the plasma ablated directly from the

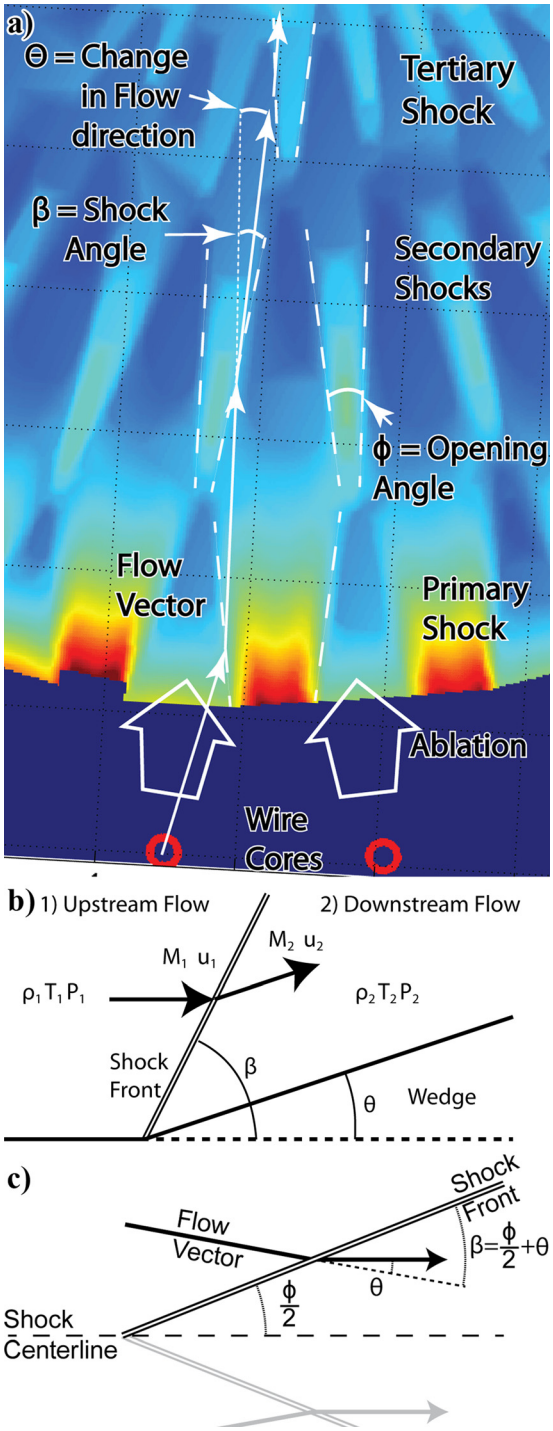

FIG. 6. (a) Schematic overlay of the oblique shock structures observed in the 32 wire aluminium array data. (b) Diagram of the geometry of an oblique shock. (c) Diagram showing angles used in the analysis of the oblique shocks observed in the experimental data.

wire core and the primary shock region, where the angle of incidence on the shock varies continuously along the full length of the shock front. By taking measurements of the observed shock geometry and applying the oblique shock relations,[22] it is possible to estimate the Mach number of the incoming flow.

Fig. 6(b) shows a diagram of the geometry of an oblique shock. The flow enters from the left side of this diagram, encountering a wedge-like obstruction which forces it to turn by some angle θ. The flow turns over a narrow shock front, formed at an angle β from the initial flow vector. This shock front divides the flow into two distinct regions (1) the upstream and (2) the downstream flow. Each region is described by a separate set of fluid state variables; temperature (T), pressure (P), density (ρ), flow velocity (u), and Mach number (M).

The angle at which the shock forms (β) is controlled by the upstream Mach number (M_1), the turning angle of the flow (θ), and the adiabatic index of the fluid (γ). The equation relating these parameters is known as the $\beta - \theta - M$ relation.[22] Rearranging this relation allows us to express M_1 in terms of, θ, β and γ

$$M_1 = \sqrt{\frac{2(\cot\beta + \tan\theta)}{\sin 2\beta - \tan\theta\,(\gamma + \cos 2\beta)}} \tag{5}$$

In order to apply this relation to the shock fronts observed in the data we first need to identify the angles θ and β. In Fig. 6(b), the formation of the shock was caused by a wedge like obstruction which forced the flow to change direction. For the oblique shocks observed in our data, the geometry is better represented by the diagram in Fig. 6(c). Instead of a wedge, the change in the flow direction is caused by the oblique collision of two adjacent radially converging supersonic ablation flows. The angle at which the two flows meet is $360°/N$, set by the array geometry and number of wires (N). After the collision the two flows travel onwards together as a single parallel flow. Invoking symmetry arguments we find that each flow must therefore turn by an angle $\theta = 360°/2N$. Whilst it is difficult to measure the shock angle (β) directly from the data, we can readily measure the opening angles of the secondary shock regions. This angle has been labelled ϕ in the diagrams in Fig. 6. We define it as the angle between the pair of shock fronts bounding each "secondary" shock region. As we have already stated, β is defined as the angle between the shock front and the initial flow vector. Inspection of the geometry shown in Fig. 6(c) reveals that we can calculate the shock angle using the following equation:

$$\beta = \frac{\phi}{2} + \theta \tag{6}$$

For a cylindrical wire array of 32 wires, the turning angle associated with each oblique shock front is $\theta = 360°/64 = 5.625°$. Measurements of the opening angle were taken for 19 of the secondary shocks in Fig. 4(b). The angle measured was somewhat dependent on the method of measurement. The largest possible angle measured was $\sim 14°$. This was obtained by measuring the angles between the points of the secondary shocks and the points of the tertiary shocks. The smallest angle was $\sim 11°$, measured by directly measuring the angles of the shock fronts from the data. The secondary shocks observed in the data have slightly blunted tips, which cause confusion with the interpretation of these angles. The resulting mean and error for these measurements are therefore $\bar{\phi} = 12.5 \pm 1.5°$, and the corresponding mean shock angle is $\bar{\beta} = 11.9 \pm 0.8°$.

The value of the effective adiabatic index (γ) for the plasma is not known, however, the range of physical values for this parameter is limited to the range $\gamma = 1 \rightarrow 5/3$. Fig. 7(a) contains a plot of the Mach number as calculated using Eq. (5) over this full range of γ, using the values for θ and β above. The plot illustrates the relatively weak dependence of this parameter on γ at this angle of incidence. The Mach number varies over the range $M_1(\beta, \gamma) = 6.2(12.6, 1) \rightarrow 9.2(11.1, 5/3)$, corresponding to both the full range of possible γ and the quoted error range for our measurement of ϕ. The results of the full set of calculations carried out for this analysis are shown in Table I.

The above estimate of M_1 may be further refined by calculating the expected value of γ for an ionising aluminium plasma using the equations described in the text book High-Energy Density Physics:[23]

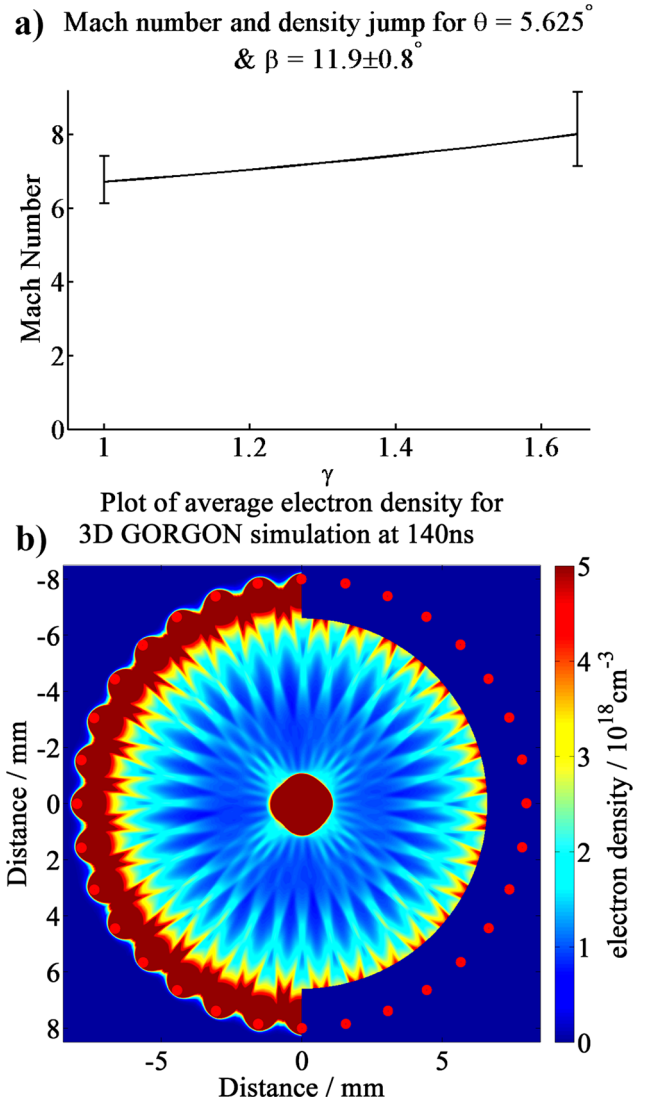

FIG. 7. (a) Plot of the incoming Mach number (M_1) for 32 wire aluminium array with varying adiabatic index (γ). This line was calculated using the oblique shock relations. (b) Plot of the axially averaged end-on electron density profile produced by a 3D Gorgon simulation of a 32 wire Al wire array. The right half of this plot is masked to match the experimental field of view. Positions of wire cores are marked with red circles.

$$\begin{aligned} \gamma &= 1 + \frac{p}{\rho_\epsilon} \\ p &= 1.6 \times 10^{-12} n_i T_e \left(1 + 0.63\sqrt{T_e} - 2.76 \times 10^{-8} n_i^{\frac{1}{3}}\right) \\ \rho_\epsilon &= 1.6 \times 10^{-12} n_i \left[1.43\sqrt{T_e} + 4.2 T_e \right. \\ &\quad \left. + T_e^{\frac{3}{2}} \left(1.3 - 0.315 \ln\left(\frac{n_i}{10^{23} T_e}\right)\right)\right]. \end{aligned} \tag{7}$$

Calculations were performed using these equations over a temperature range of $10 \rightarrow 30$ eV and ion density range of $10^{16} \rightarrow 10^{18}$ cm^{-3}, resulting in the range of $\gamma = 1.09 \rightarrow 1.13$. If this range of γ is accurate then we can reduce the range for the estimate for the Mach number to M_1 (β, γ) = 6.3(12.6, 1.1)$\rightarrow$7.7(11.1, 1.13). The width of this range is dominated by the error in the determination of the shock angle. Again further details of these calculations are given in Table I.

It should, however, be noted that the equation we have used to calculate γ here is derived using a very much simplified model, and thus the true value of γ may be somewhat different. The important point is that energy loss due to the ionisation of the plasma will reduce the effective value of γ significantly compared to the ideal gas value of 5/3. Thus, we should not expect the real value of the Mach number to fall near the top of the full range given above.

C. Comparisons with Mach number obtained from Gorgon simulations

Fig. 7(b) shows a plot of the axially averaged end-on electron density distribution taken from a simulation of a 32 wire aluminium cylindrical wire array using the 3D resistive MHD code Gorgon.[15,16] A mask has been placed over the right half of this plot to indicate the field of view corresponding to the interferograms in Fig. 4. The overall structure of the simulated data appears similar to that seen in the experimental data, allowing the same analysis process to be applied to the simulated shocks. Measurements of the opening angles (ϕ) for the secondary shocks, taken from the plot in Fig. 7(b), based on the geometry shown in Fig. 6(c), resulted in an average opening angle of $\phi \sim 14.04 \pm 0.4°$. This measurement falls just at the upper limit of the angles we determined from the experimental data. The collision angle remains $\theta = 5.625°$, resulting in a shock angle of $\beta = 12.6 \pm 0.2°$. The γ of the numerical plasma is not known. Inserting these values of θ and β into Eq. (5), and calculating over the full range of possible γ, allows us to estimate a range for the Mach number. The variation in this range is dominated by the uncertainly in the plasma γ, $M_1(\gamma) \sim 6.0\ (1) \rightarrow 7.4(5/3)$ This range appears to agree well the experimental data presented in Sec. II.

The simulations also give us access to other plasma parameters, allowing us to calculate the expected Mach number directly.[24] For the following calculation, we selected a point at a radius r = 5 mm; corresponding to the region where collisions take place between the primary and secondary flows. The plasma parameters taken from the simulation at this point were $T_e \sim 8$ eV, $\bar{Z} \sim 5$ and ablation flow velocity $v_{flow} = 8.5 \times 10^6$ cm s^{-1}. The Mach number ($M = v_{flow}/c_s$),

TABLE I. Detail summary of the results of calculations carried out during the analysis of the shock structures in 32 wire aluminium arrays presented in this paper.

Parameter		γ			
Experiment:	β	1	1.09	1.13	5/3
M_1 (For primary shock region, based on geometry.)	11.1°	7.4	7.6	7.7	9.2
	12.6°	6.2	6.3	6.4	7.3
$\bar{Z}T_e$ – Ranges: (For v_{flow}=8→11×10^{6}cm^{-3} β=11.1→12.6°)		32→89eV	28→79eV	27→74eV	13→39eV
Gorgon Simulation:					
M_1 (For primary shock region, based on measurements of the geometry.)		6.0	6.1	6.5	7.4
M_1 (For primary shock region, based on fluid parameters.)		7.1	6.8	6.7	5.5

was calculated, using the ion sound speed ($c_s = \sqrt{\gamma \bar{Z} k_B T_e / m_i}$), over the full range of γ, resulting in a range of possible Mach numbers $M \sim 7.1$ ($\gamma = 1$) → 5.4 ($\gamma = 5/3$). More detailed results of these calculations are shown in Table I. For this calculation, M decreases with γ, whereas for the calculation from the geometry M increases with γ, thus we can use the equations to try to estimate the effective γ of the simulated plasma. By adjusting γ in order to match the resulting M's, we get $\gamma = 1.16$, and $M = 6.4$. This value of γ agrees reasonably well with the range we estimated earlier ($\gamma = 1.09 \rightarrow 1.13$). The value for the M falls towards the bottom of the range of values we have estimated from the experimental data.

Ionisation calculations in Gorgon are performed using a Thomas-Fermi model. This is a local thermodynamic eEquilibrium (LTE) model, designed for application at much higher densities, and tends to over-estimate the ionisation state of lower density plasmas. The ionisation model used in Gorgon is currently an area of active work and improved modelling has recently been presented at a number of conferences.[25,26] In order to investigate the effect of this change in ionisation state of the plasma, a number of simulations were run using the new Non-Local Thermodynamic Equilibrium (NLTE) model. While this model did predict significantly reduced ionisation ($\bar{Z} \approx 3.6$ in the region of interest disgusted above), it also predicted higher temperatures in the flow. The overall result was that the $\bar{Z}T_e$ of the plasma did not change significantly. The shock angles measured from the resulting density maps therefore only showed a minimal reduction in the opening angle ($\phi \approx 13.5°$). The reduction does, however, agree better with the experimental data.

D. Estimate of ZT_e based on the Mach number and Thomson scattering velocity measurements

The experimental determination of the Mach number based on the shock geometry, developed in Sec. III B), can be used in combination with recently published flow velocity measurements from Thomson scattering experiments[27,28] to further investigate the parameters of the aluminium ablation plasma. Fig. 8 shows plots of the radial velocity profiles measured for both 16 and 32 wire aluminium arrays taken from a paper by Harvey-Thompson *et al.*[28] In these experiments, the Thomson scattering beam was aligned through a pair of opposing inter-wire gaps, such that the velocities measured for the 32 wire arrays should correspond directly to the flow velocity in the primary shock region, the same region for which we have calculated the Mach number. The range of radii over which our determination of the Mach number is relevant is r~3-5 mm. The corresponding range of the flow velocity, as measured by Thomson scattering, taken from the plot in Fig. 8, is $\sim 8 \rightarrow 11 \times 10^6$ cm s^{-1}. Using the equation for the ion sound speed and our earlier determination of the range for the Mach number, we can estimate a range for the $\bar{Z}T_e$ of the plasma (the product of the electron temperature and the average ionisation). For $\gamma = 1$ we get $\bar{Z}T_e = 32 \rightarrow 90$ eV and for $\gamma = 5/3$ $\bar{Z}T_e = 13 \rightarrow 38$ eV. As already discussed, we expect γ to lie somewhere towards the bottom of its full range. Using the reduced range of γ calculated in Sec. III B, $\gamma = 1.09 \rightarrow 1.13$, results in a reduced estimated range for $\bar{Z}T_e = 27 \rightarrow 78$ eV.

E. Shock structure in 16 wire aluminium arrays

The electron density structures produced by 16 wire aluminium arrays (Fig. 4(a)) are more complicated to interpret than those produced by the 32 wire arrays. Shocked regions are still present in the interwire gaps between the ablation streams but are of lower density relative to the ablation streams themselves. This is because the interwire gap is larger; ablated plasma must travel further to reach the centreline, and thus less material has entered the primary shock at this radius. The data provide a lower limit for the expansion of the ablation streams, estimated based on the observation

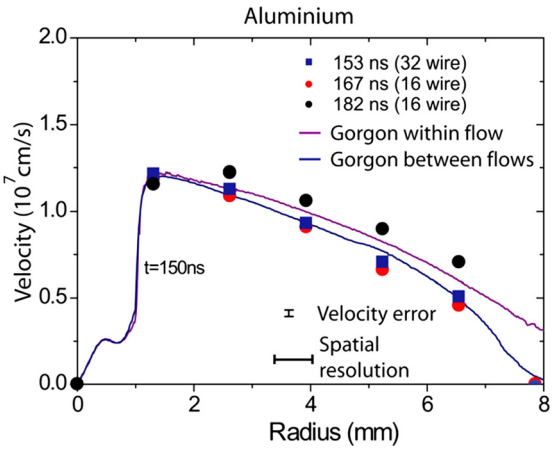

FIG. 8. Ablation flow velocity with radius for 16 and 32 wire arrays, as measured by Thomson scattering. Gorgon simulated velocities are included for comparison. Reprinted with permission from A. J. Harvey-Thompson, S. V. Lebedev, S. Patankar, S. N. Bland, G. Burdiak, J. P. Chittenden, A. Colaitis, P. De Grouchy, G. N. Hall, E. Khoory, M. Hohenberger, L. Pickworth, F. Suzuki-Vidal, R. A. Smith, J. Skidmore, L. Suttle, and G. F. Swadling, Phys Plasmas **19**, 056303 (2012). Copyright 2012 American Institute of Physics.

of the formation of shocks in the interwire gaps. This lower limit of ~2.6 mm is slightly greater than the expansion observed in the 7 wire data shown in Fig. 5. This increase in the expansion of the flow for larger wire number may be due to the reduction in the local field around each wire. This local magnetic field may induce a pinching effect, acting to focus the stream for sufficiently large interwire gaps.

Fig. 9 shows an annotated and expanded view of a region of the data from Fig. 4(a). This view clearly shows that the regions of enhanced density between the ablation streams are again bounded by oblique shock fronts. The formation mechanism for this "primary" shock region is assumed to be similar to that discussed above for the 32 wire case. The increased azimuthal separation between the flows means that the "primary" shock regions do not meet one another before the probe beam is obscured, and as a result the formation of "secondary" shock regions is not observed.

Following the "primary shock" towards the axis in Fig. 9 reveals a different evolution of the structure compared with the 32 wire case. The region develops a hollow structure, with a higher density at the edges and lower density towards the centreline. This structure may be due to a variation in the temperature of the plasma across the region; a higher temperature could provide the pressure balance required to stabilise the low density region. The variation in temperature could be caused by changes in the angle of incidence for material impacting the shock front. The material colliding at large radius, which forms the core of the shock region, impacts the shock front with a greater angle of incidence. A larger fraction of its kinetic energy must therefore be stagnated across the shock front, resulting in higher temperature post-shock plasma. Further towards the axis the flows collide into the shock at a smaller angle of incidence, resulting in a smaller stagnation fraction and thus a lower temperature.

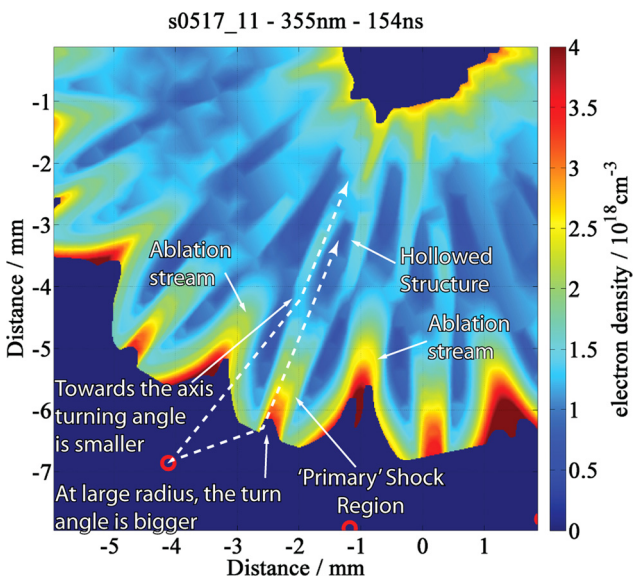

FIG. 9. Annotated expanded view of 16 wire Aluminium array data, showing hollow structure of the primary shocks. It is thought that the hollow structures form due to variations in the plasma temperature, driven by the changing angle of incidence of plasma impinging on the shock front.

A careful inspection of the 32 wire data in Figs. 4(b) and 6(a) reveals similar hollow structures in the primary shock regions, however, this hollowed profile is not observed in the other shock regions. This might be expected, as there should be no variation in the angle of incidence for material impacting the secondary and tertiary shocks, and thus no temperature variation.

F. Evidence of reduced collisionality at early times in the 16 wire array data

Fig. 10 shows electron density plots from two separately timed interferograms taken from the same 16 wire aluminium array experiment. Fig. 10(a) was captured at 107 ns and Fig. 10(b) 28 ns later. In the earlier frame, there is no visible evidence of the formation of collisional structures. No shocks

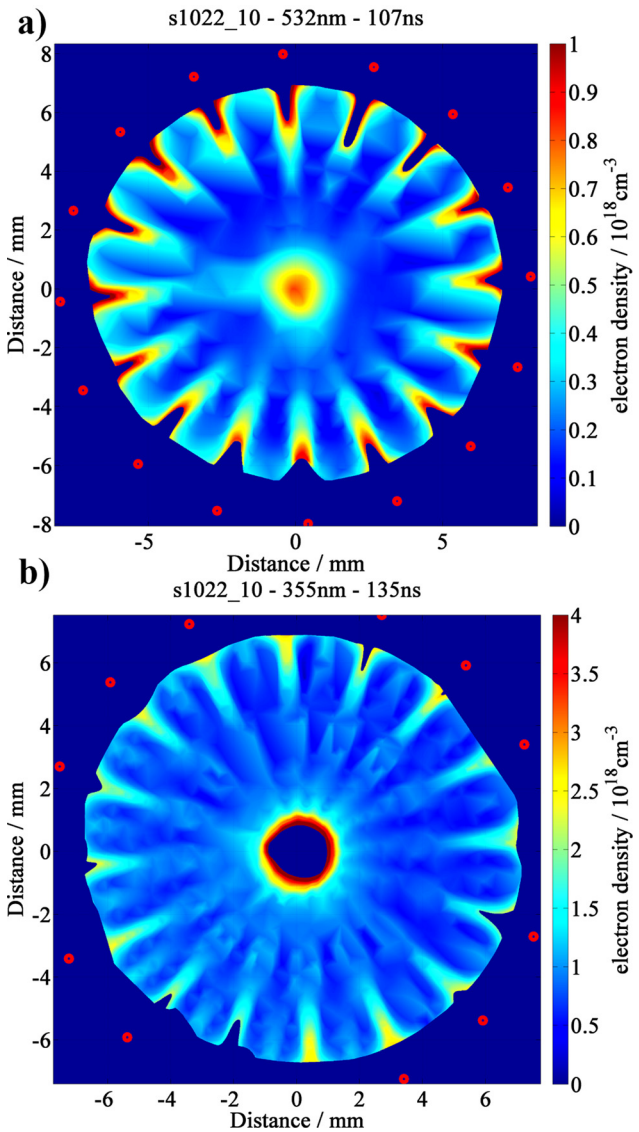

FIG. 10. Electron density distributions for a 16 wire array. Red spots indicate the initial wire positions (a) Data from the 532 nm interferogram, captured at 107 ns from current start. Collisional structures are not observed. The distribution of precursor plasma about the axis appears isotropic and no shocks are observed in the interwire-gaps. (b) Data from the 355 nm interferogram, captured at 135 ns. There is now evidence of the formation of the collisional features, such as shocks between ablation streams and structure around the axis.

are observed in the interwire gaps and the distribution of plasma on axis appears isotropic. In the later frame, there is clear evidence of the shock structures described in the previous sections, and although the axis has become too dense to be probed, there is clear evidence of azimuthal structure around its edges. This delayed onset of collisional features demonstrates that the plasma flow has undergone a transition of its collisional dynamics.

The collisional mechanics of plasmas are discussed in some detail by Trubnikov,[29] in which equations are derived for calculating the collisional frequencies corresponding to a range of changes to the velocity distribution function of the plasma. These equations are summarised in the NRL plasma physics formulary.[24] For the following calculations, we have used the "slowing down" frequency, $\nu_s^{\alpha/\beta}$ which is defined

$$\frac{d\vec{v}_\alpha}{dt} = -\nu_s^{\alpha/\beta}\vec{v}_\alpha, \tag{8}$$

where $\nu_s^{\alpha/\beta}$ is the exponential time constant describing the average deceleration rate of a group of test particles, labelled α, traveling with initial velocity $\vec{v}_\alpha$ through a static field of thermal scattering particles, labelled β. This parameter is calculated using the following equation:

$$\nu_s^{\alpha/\beta} = \left(1 + \frac{m_\alpha}{m_\beta}\right)\psi(x^{\alpha/\beta})\nu_0^{\alpha/\beta}, \tag{9}$$

where m_α and m_β are the masses of the two types of particles, $\psi(x)$ is the velocity potential of the interaction and $\nu_s^{\alpha/\beta}$ is the coulomb collision frequency, given by the following equation (in CGS units):

$$\nu_0^{\alpha/\beta} = \frac{4\pi e_\alpha^2 e_\beta^2 \lambda_{\alpha\beta} n_\beta}{m_\alpha^2 v_\alpha^3} \tag{10}$$

where e^α and e^β are the average charges of the two sets of particles, n_β is the β particle density and v_α is relative velocity of the α particles. $\lambda_{\alpha\beta}$ is the coulomb logarithm, a factor describing the relative importance of large-angle single interaction events compared to multiple long-range small-angle interactions.

The collisional scale length can be estimated based on the time constant for deceleration using the following expression:

$$l_s^{\alpha/\beta} = \frac{\vec{v}_\alpha}{\nu_s^{\alpha/\beta}}. \tag{11}$$

For strongly collisional dynamics to be observed, we expect the collisional scale length to be much smaller than the experimental scale length. At the very most it should be expected that $l_s^{\alpha/\beta}$ should be of the same order as the widths of the shock fronts observed in the 32 wire experiments discussed earlier, $\sim 100\,\mu$m.

Calculations using the above equations reveal that for the aluminium wire array plasmas discussed in this paper the collisional effects are dominated by the ion-ion interactions between the flows ($l_s^{i/e} \sim 10^2 l_s^{i/i}$). In the 16 wire case, for an electron density of $\sim 10^{16}\,\mathrm{cm}^{-3}$ and electron temperature of $\sim 20\,\mathrm{eV}$, $l_s^{i/i} \sim 1\,\mathrm{mm}$, while at $\sim 10^{17}\,\mathrm{cm}^{-3}$ this falls to $100\,\mu$m.

Ignoring the effects of the velocity potential (ψ) and the coulomb logarithm ($\lambda_{\alpha\beta}$), a cursory examination of Eqs. (10) and (11) reveals that $l_s^{\alpha/\beta}$ scales inversely with n_β. This is most likely to be the scaling that causes the change in the collisionality observed in the 16 wire array data in Fig. 10, as the density of the plasma increases by at least an order of magnitude between the two frames. $l_s^{\alpha/\beta}$ also scales quadratically with e_α and e_β, and quadratically with the α particle kinetic energy ($E_\alpha = m_\alpha v_\alpha^2/2$). In the case of the ablation stream interactions, the α and β particles will be of the same species and thus $l_s^{i/i}$ will be scale as $\bar{Z}^{-4}$. This strong dependence illustrates the importance of correctly modelling the ionisation of the plasma. The quadratic scaling with kinetic energy means $l_s^{\alpha/\beta}$ also scales with v_α^4. For collisions between adjacent streams the approach velocity is calculated using the following expression: $v_\alpha = v_{Abl}\tan(\pi/N)$ ($\sim v_{Abl}\pi/N$ for large N). From this expression, we see that if we can assume that the ablation velocity is reasonably independent of the wire number of the array, then as the wire number increases the collision velocity will trend as N^{-1}, and thus $l_s^{\alpha/\beta}$ for interactions between streams will trend down as n^{-1} ($l_s^{\alpha/\beta} \propto N^{-4}$). This effect appears to be borne out by data from 32 wire arrays, as the full collisional structures have been observed in an interferogram captured at 114 ns for this wire number. For wire arrays with much larger wire numbers, it should be expected that the plasma will be collisional at even earlier times.

IV. CONCLUSIONS

The data presented in this paper demonstrate the strongly collisional nature of aluminium wire array ablation flow plasma at the 1.4 MA current scale on MAGPIE. Analysis of the shock structures formed due to the interaction of adjacent ablation flows as they converge toward the axis can inform us about various parameters of the plasma, such as the Mach number in these flows. The results of the analysis carried out in this paper are summarised in Table I. Measurement and analysis of the oblique shock angles allowed us to estimate the Mach number of the ablation flow in a 32 wire aluminium array experiment. The estimated range was $M_1 = 6.2 \rightarrow 9.2$. Combining this estimate with previously published measurements of the flow velocity taken from Thomson-Scattering experiments[28] allowed us to estimate a range for the $\bar{Z}T_e$ of the plasma, 13-89 eV. These ranges make no assumptions about the value of γ for the plasma, however, earlier calculations using an ionising plasma model[23] allowed us to estimate a smaller range for this parameter, $\gamma \sim 1.09$-1.13. Assuming this range is accurate, we can reduce the range of our estimates for both M_1 and $\bar{Z}T_e$ significantly. In this case, $M_1 = 6.3$-7.7, and correspondingly $\bar{Z}T_e = 27$–79 eV.

It is expected that the azimuthal structure of the electron density will be accompanied by a corresponding structure in the array mass distribution, with changes in the relative density being due only to variations in the plasma average ionisation ($\bar{Z}$). The resulting azimuthal and radial modulation of the array pre-fill density will cause a variation in the radially integrated prefill mass, which could induce perturbations in

the implosion-front, resulting in reduced peak radiative power due to an increase in the total stagnation time. It is doubtful, however, that this effect would dominate, as it is unlikely to be stronger than the axial modulations caused by the magneto-Rayleigh-Taylor instability, which has been shown to dominate array implosion dynamics.[4,30] Also, as the wire number of the arrays increases, the increasing numbers of shocks will at to effectively smooth out the radially integrated mass perturbations.

Comparison of the experimental data presented in this paper with the results of numerical modelling may be useful for code benchmarking or model validation exercises. The detailed data on shock geometry which can be extracted from the electron density plots are sensitive to many different physical parameters of the plasma. We have demonstrated that Gorgon modelling reproduces the overall structure of the ablation plasma. The shock angles measured from the simulation fall within the errors of those measured from the experimental data.

Finally, it should be noted that the work presented in this paper covers only the results of experiments on aluminium wire arrays. Experiments have been performed which demonstrate that the dynamics of tungsten wire arrays are significantly different at the MAGPIE 1.4 MA current scale. For these arrays, the collisional scale lengths of the ablation streams become large enough that the plasma no longer behaves as a fluid, resulting in much more drastic discrepancies between experiment and simulation. The results and analysis of these experiments will form the basis of a future publication.

ACKNOWLEDGMENTS

This work was supported by AWE, by EPSRC Grant No. EP/G001324/1 and by the NNSA under DOE Cooperative Agreement Nos. DE-F03-02NA00057 and DE-SC-0001063.

[1]M. G. Haines, Plasma Phys. Controlled Fusion **53**, 093001 (2011).
[2]C. Deeney, M. Douglas, R. Spielman, T. Nash, D. Peterson, P. L'Eplattenier, G. Chandler, J. Seamen, and K. Struve, Phys. Rev. Lett. **81**, 4883 (1998).
[3]S. V. Lebedev, F. N. Beg, S. N. Bland, J. P. Chittenden, A. E. Dangor, M. G. Haines, K. H. Kwek, S. A. Pikuz, and T. A. Shelkovenko, Phys. Plasmas **8**, 3734 (2001).
[4]M. E. Cuneo, E. M. Waisman, S. V. Lebedev, J. P. Chittenden, W. A. Stygar, G. A. Chandler, R. A. Vesey, E. P. Yu, T. J. Nash, D. E. Bliss, G. S. Sarkisov, T. C. Wagoner, G. R. Bennett, D. B. Sinars, J. L. Porter, W. W. Simpson, L. E. Ruggles, D. F. Wenger, C. J. Garasi, B. V. Oliver, R. A. Aragon, W.E. Fowler, M. C. Hettrick, G. C. Idzorek, D. Johnson, K. Keller, S. E. Lazier, J. S. McGurn, T. A. Mehlhorn, T. Moore, D. S. Nielsen, J. Pyle, S. Speas, K. W. Struve, and J. A. Torres, Phys. Rev. E **71**, 1 (2005).
[5]V. V. Aleksandrov, Plasma Phys. Rep. **27**, 89 (2001).
[6]S. V. Lebedev, R. Aliaga-Rossel, S. N. Bland, J. P. Chittenden, A. E. Dangor, M. G. Haines, and I. H. Mitchell, Phys. Plasmas **6**, 2016 (1999).
[7]S. Lebedev, F. Beg, S. Bland, J. Chittenden, A. Dangor, M. Haines, S. Pikuz, and T. Shelkovenko, Phys. Rev. Lett. **85**, 98 (2000).
[8]S. V. Lebedev, F. N. Beg, S. N. Bland, J. P. Chittenden, A. E. Dangor, and M. G. Haines, Phys. Plasmas **9**, 2293 (2002).
[9]D. D. Ryutov, M. Derzon, and M. Matzen, Rev. Mod. Phys. **72**, 175 (2000).
[10]C. Deeney, T. Nash, R. Spielman, J. Seaman, G. Chandler, K. Struve, J. Porter, W. Stygar, J. McGurn, D. Jobe, T. Gilliland, J. Torres, M. Vargas, L. Ruggles, S. Breeze, R. Mock, M. Douglas, D. Fehl, D. McDaniel, M. Matzen, D. Peterson, W. Matuska, N. Roderick, and J. MacFarlane, Phys. Rev. E **56**, 5945 (1997).
[11]R. B. Spielman, C. Deeney, G. A. Chandler, M. R. Douglas, D. L. Fehl, M. K. Matzen, D. H. McDaniel, T. J. Nash, J. L. Porter, T. W. L. Sanford, J. F. Seamen, W. A. Stygar, K. W. Struve, S. P. Breeze, J. S. McGurn, J. A. Torres, D. M. Zagar, T. L. Gilliland, D. O. Jobe, J. L. McKenney, R. C. Mock, M. Vargas, T. Wagoner, and D. L. Peterson, Phys. Plasmas **5**, 2105 (1998).
[12]I. H. Mitchell, J. M. Bayley, J. P. Chittenden, J. F. Worley, A. E. Dangor, M. G. Haines, and P. Choi, Rev. Sci. Instrum. **67**, 1533 (1996).
[13]S. V. Lebedev, R. Aliaga-Rossel, J. P. Chittenden, I. H. Mitchell, A. E. Dangor, M. G. Haines, and J. F. Worley, Phys. Plasmas **5**, 3366 (1998).
[14]S. Bott, S. Lebedev, D. Ampleford, S. Bland, J. Chittenden, A. Ciardi, M. Haines, C. Jennings, M. Sherlock, G. Hall, J. Rapley, F. Beg, and J. Palmer, Phys. Rev. E **74**, 1 (2006).
[15]A. Ciardi, S. V. Lebedev, A. Frank, E. G. Blackman, J. P. Chittenden, C. J. Jennings, D. J. Ampleford, S. N. Bland, S. C. Bott, J. Rapley, G. N. Hall, F. A. Suzuki-Vidal, A. Marocchino, T. Lery, and C. Stehle, Phys. Plasmas **14**, 056501 (2007).
[16]J. P. Chittenden, S. V. Lebedev, C. A. Jennings, S. N. Bland, and A. Ciardi, Plasma Phys. Controlled Fusion **46**, B457 (2004).
[17]C. Deeney, T. J. Nash, R. B. Spielman, J. F. Seaman, J. S. McGurn, D. O. Jobe, M. F. Vargas, T. L. Gilliland, R. C. Mock, K. W. Struve, K. G. Whitney, P. E. Pulsifer, J. P. Apruzese, J. W. Thornhill, and J. Davis, Phys. Plasmas **5**, 2431 (1998).
[18]G. F. Swadling, "An experimental investigation of the azimuthal structures formed during the ablation phase of wire array z-pinches," Ph.D. dissertation (Imperial College, 2012).
[19]I. H. Hutchinson, *Principles of Plasma Diagnostics* (Cambridge University Press, 2005).
[20]J. Chittenden and C. Jennings, Phys. Rev. Lett. **101**, 1 (2008).
[21]A. J. Harvey-Thompson, S. V. Lebedev, S. N. Bland, S. C. Bott, J. P. Chittenden, G. N. Hall, C. Ning, F. Suzuki-Vidal, B. R. Kusse, and D. a. Hammer, in *AIP Conference Proceedings* (AIP, 2009), pp. 105–108.
[22]J. Anderson, *Modern Compressible Flow: With Historical Perspective* (McGraw-Hill Companies,Incorporated, 2002).
[23]R.P. Drake, *High-Energy-Density Physics: Fundamentals, Inertial Fusion, and Experimental Astrophysics* (Springer, 2006).
[24]D. Book and J. D. Huba, *NRL Plasma Physics Formulary* (NRL, 2002), pp. 24, 29, and 31–39.
[25]N. P. L. Niasse and J. P. Chittenden, in talk given at 2012 ICOPS Conference, Edinburgh, UK (2012).
[26]N. P. L. Niasse, in 2011 DZP Conference, Biarritz, France (2011).
[27]A. Harvey-Thompson, S. Lebedev, S. Patankar, S. Bland, G. Burdiak, J. Chittenden, A. Colaitis, P. De Grouchy, H. Doyle, G. Hall, E. Khoory, M. Hohenberger, L. Pickworth, F. Suzuki-Vidal, R. Smith, J. Skidmore, L. Suttle, and G. Swadling, Phys. Rev. Lett. **108**, 145002 (2012).
[28]A. J. Harvey-Thompson, S. V. Lebedev, S. Patankar, S. N. Bland, G. Burdiak, J. P. Chittenden, A. Colaitis, P. De Grouchy, G. N. Hall, E. Khoory, M. Hohenberger, L. Pickworth, F. Suzuki-Vidal, R. A. Smith, J. Skidmore, L. Suttle, and G. F. Swadling, Phys. Plasmas **19**, 056303 (2012).
[29]B. A. Trubnikov, Rev. Plasma Phys. **1**, 105 (1965).
[30]D. B. Sinars, M. E. Cuneo, B. Jones, C. a. Coverdale, T. J. Nash, M. G. Mazarakis, J. L. Porter, C. Deeney, D. F. Wenger, R. G. Adams, E. P. Yu, D. E. Bliss, and G. S. Sarkisov, Phys. Plasmas **12**, 056303 (2005).